Journal of Sol-Gel Science and Technology
https://doi.org/10.1007/s10971-025-06724-6

ORIGINAL PAPER

Hybrid silica aerogels from bridged silicon alkoxides: ultralow thermal conductivity for low-temperature applications

A. M. Abebe[1] · M. Biesuz[1] · C. Vakifahmetoglu[2] · M. Cassetta[1,3] · G. D. Sorarù[1]

Received: 23 December 2024 / Accepted: 28 February 2025

Abstract

Hybrid silica aerogels are promising materials for thermal insulation applications. Highly porous aerogels were synthesized from bridged bis(triethoxysilyl)methane BTEM and triethoxysilane TREOS silicon alkoxides via the sol–gel process. The carbon content in the hybrid aerogels decreased with increasing amounts of TREOS. Crack-free monolith aerogels were synthesized through supercritical drying, which is crucial for thermal and optical investigations. The aerogels are characterized by high BET surface areas ranging from 700 to 1400 m²/g, pore volumes between 2.0 and 10.5 cm³/g, and a maximum porosity of 95%. The thermal conductivity of the aerogels at room temperature was measured via a hot disk apparatus. The materials exhibited ultralow thermal conductivity, reaching a minimum value of 15 mW/mK. This value ranks among the lowest reported values for silica-based aerogels in the literature. Optical transmittance measurements indicated high transparency, exceeding 80% in the visible region. Therefore, these exceptional properties of low density, high optical transparency, and low thermal conductivity make these materials promising candidates for transparent insulation applications.

Graphical Abstract

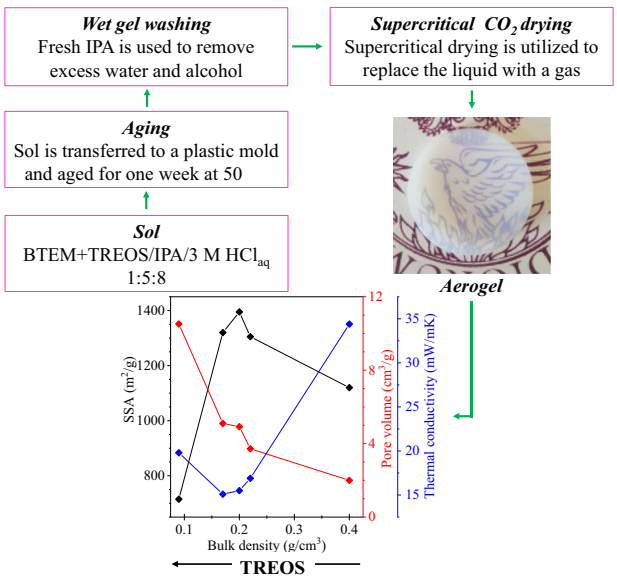

✉ A. M. Abebe
adanemuche.abebe@unitn.it

[1] Department of Industrial Engineering, University of Trento, Via Sommarive 9, 38123 Trento, Italy

[2] Department of Materials Science and Engineering, Izmir Institute of Technology, Izmir, Turkey

[3] Department of Engineering for Innovation Medicine, University of Verona, 37134 Verona, Italy

Published online: 17 March 2025

Keywords Hybrid aerogel · Sol-gel · Optical transmittance · Low thermal conductivity · High surface area

Highlights

- Highly porous hybrid aerogels were synthesized *via* the sol-gel process and supercritical CO_2 drying.
- The bulk density, shrinkage, and pore volume of the aerogels are influenced by the amount of TREOS.
- The BT2 aerogel achieved a minimum thermal conductivity of 15 mW/mK with a bulk density of 0.17 g/cm^3
- The BT2 aerogel demonstrated 80% transmittance at a wavelength of 550 nm.

1 Introduction

An aerogel is a mesoporous solid consisting of a network of nanosized particles. It was first produced by Samuel Kistler in 1932 by removing the liquid phase of a gel via supercritical drying [1]. Aerogels are characterized by their high surface area (250−1000 m^2/g) [2], high porosity (80–99.8%) [3–5], low density (0.03–0.50 g/cm^3) and ultralow thermal conductivity (15–50 mW/m-K) [6–10]. These outstanding properties are derived from their unique nanostructure, which consists of a three-dimensional network of nanoparticles and submicron pores. Consequently, aerogels are promising materials for various applications, including sorbents, catalysis carriers, energy storage, filters and thermal insulators.

Silica aerogels, obtained via the sol–gel process from tetraethyl orthosilicate (TEOS), are among the most studied aerogel materials [11, 12]. They have gained significant attention because of their lightweight nature, large specific surface area and high porosity. These properties make silica aerogels commercially valuable in various applications, such as residential buildings [13–16], solar power towers [17] and construction industries [5, 18], particularly because of their low thermal conductivity and optical transparency. Silica-based aerogels can also be synthesized from hybrid silicon alkoxides, $R_xSiO_{(2-x)/2}$, where R represents an organic group (CH_3, CH_2CH_3, $CH=CH_2$, C_6H_5, or H). These precursors impart flexibility, strength, or additional functionalities to the resulting silica-based aerogels, thereby broadening their potential applications in the energy, environmental, and optoelectronic fields [19–21].

Transparent silica-based aerogels have gained significant interest due to their high optical transmittance and extremely low thermal conductivity [22, 23]. They serve as optical filters, allowing sunlight to penetrate while absorbing infrared radiation [24]. Ultralow thermal conductivity was achieved by suppressing solid- and gas-phase thermal transport, ensuring values lower than ambient air [14, 25]. These remarkable properties make the aerogels one of the promising candidates for applications requiring transparency and thermal insulation, such as roofs, window panels and solar collector covers.

In this work, we report the synthesis of highly porous hybrid silica aerogels obtained via the co-hydrolysis of bridged (bis(triethoxysilyl)methane (BTEM) and triethoxysilane (TREOS) in varying proportions. The hybrid aerogels containing the methylene bridge, exhibit a high surface area (∼1100 m^2/g) and small voids (mesopores ∼15 nm in diameter) [26], which improves the mechanical strength of the final aerogels. Furthermore, the BTEM/TREOS system is noteworthy for its potential as a precursor for transparent silicon oxycarbide ceramic aerogels [27]. In this context, the TREOS precursor, which contains only Si-H bonds and no Si-C bonds, is used to modulate the carbon content. This ensures that, after pyrolysis, a stoichiometric silicon oxycarbide glass free of excess carbon (C_{free}) can be obtained. The study of this precursor's pyrolysis and the characterization of the resulting SiOC glass will be reported in another paper.

The primary objective of the present study is to characterize low-carbon transparent hybrid silica aerogels and investigate how composition variations influence their microstructure, as well as their optical and thermal properties.

2 Experimental techniques

2.1 Aerogel synthesis

Two types of Si-containing alkoxides were employed to synthesize highly porous aerogels. Bis(triethoxysilyl) methane (BTEM, CAS: 18418-72-9) was purchased from Fluorochem Chemicals (Hadfield, UK), and triethoxysilane (TREOS, CAS: 998-30-1) was purchased from Sigma–Aldrich GmbH (95%, Steinem, Germany). Isopropanol alcohol (IPA, CAS: 67-63-0) was purchased from CARLOERBA Reagents (99.8%, Italy). Hydrochloric acid (HCl) was purchased from Sigma–Aldrich Chemicals (Steinem, Germany). All chemicals were used as received except for HCl, which was diluted from 12 M to 3 M.

Hybrid silica aerogels with BTEM/TREOS molar ratios of 1/0 (pure BTEM), 2/1, 1/1, 1/2, and 0/1 (pure TREOS) were prepared and labeled B, B2T, BT, BT2, and T, respectively. The appropriate molar quantities of BTEM

and TREOS were combined to achieve the desired compositions, and this mixture was stirred for 5 min in isopropanol via a magnetic stirrer. Afterward, acidic water (3 M HCl aqueous solution) was added to promote the hydrolysis–condensation reactions. The molar ratio of the Si alkoxides, IPA, and acidic water was (BTEM + TREOS)/IPA/H_2O = 1/5/8. Finally, the solution was cast in cylindrical plastic molds, which were left closed for gelation. The gelation time spans from a minimum of 10 min for a pure TREOS composition up to 1 h for a pure BTEM gel.

After gelation, the samples were aged for one week at 50 °C in a sealed container, and the wet gel underwent washing steps in which fresh IPA was used to remove excess water, HCl, and other chemical species produced during the hydrolysis–condensation reactions. The sample was subsequently transferred into a 50 cm^3 glass container and placed inside a custom-made supercritical CO_2 drying reactor, where the gels were washed with liquid CO_2 for three days to remove the IPA. Ultimately, the liquid carbon dioxide was brought above the critical temperature and pressure (T_{cr} = 31.1 °C and P_{cr} = 7.38 MPa) by setting the temperature to 45 °C. The pressure valve was slowly opened to allow the gradual release of pressure until it reached 1 bar. The water bath was subsequently switched off, and the temperature of the aerogel slowly decreased to room temperature, resulting in monolithic aerogel samples. Top of Form

2.2 Characterization

The bulk density (ρ_b) of the as-prepared gels was estimated through mass and volume relations, whereas their skeleton density (ρ_s) was determined via an Ultrapyc 5000 gas pycnometer (Anton Paar GmbH, Graz, Austria). The measurements were made at 20 °C with helium gas, with a target pressure of 1.24 bar, a purging time of 30 min, and a total of 30 runs. The porosities (ϕ) of the aerogel samples were subsequently computed via the following equation: $(1 - (\rho_b/\rho_s)) \times 100\%$.

Fourier transform infrared (FT-IR) spectra were recorded with a Thermo Optics Avatar 330 instrument (Thermo Fischer Scientific, Waltham, MA, USA) on thin, transparent potassium bromide (KBr) pellets. The spectra were collected in the 4000–400 cm^{-1} range in transmittance, employing peak-to-peak (the vertical intensity difference between the lowest and highest points of the peak), with 64 scans and 4 cm^{-1} resolution. The IR data provided insights into the chemical evolution of the aerogel materials before and after pyrolysis at different temperatures.

The N_2 adsorption isotherm, BET, (Brunauer, Emmett and Teller) surface area, and pore size distribution of the aerogels were characterized via a Quantachrome Instrument (Anton Paar, USA) with nitrogen as the adsorbate gas at −196 °C. Aerogel samples (20–50 mg) were used for nitrogen physisorption analysis. Before adsorption analysis, all the samples were degassed to remove all physically adsorbed impurities, such as adsorbed gases, water vapor, and other volatile substances. Degassing took place at 50 °C for 12 h. The cumulative pore volume and pore diameter were determined from the adsorption branch via density functional theory (DFT) calculations.

The microstructures of the hybrid aerogels were analyzed on fracture surfaces coated with a thin Pt/Pd (80:20) film via high-resolution scanning electron microscopy (SEM-FEG Zeiss SUPRA^{TM} 40, Germany).

The thermal conductivity of the disk-shaped aerogels (approximately 10 mm thick and 30 mm in diameter) was measured via a Hot Disk apparatus (Hot Disk TPS 2500 S, Kagaku Analys AB, Sweden). A double spiral nickel wire sensor with a 3.189 mm sensor radius was placed between two flat surface samples. Applying 3 mW of power for 160 s increased the temperature of the wire and surrounding samples. The thermal conductivity of the sample was subsequently estimated on the basis of known values of the temperature increment and initial power input.

The optical properties of a 2.5 mm thick hybrid aerogel were analyzed via a UV–Vis–NIR spectrophotometer (Jasco V770). The transmittance was measured in the 190–2500 nm range at 400 nm/min.

3 Results and discussion

3.1 Physical properties

Monolithic, crack-free preceramic aerogels - enough strong to be handled without any issues - were prepared *via* the sol–gel process and supercritical CO_2 drying. Except for the T gel, which appears opaque due to the formation of large macropores, as shown later, all the aerogels are transparent to visible light, as shown in Fig. 1. The transparent samples look bluish against a dark background owing to Rayleigh scattering, primarily in the blue region of the visible spectrum [28, 29]. Furthermore, close observation of Fig. 1 reveals that the shrinkage of the aerogel samples after supercritical drying decreases with the amount of TREOS.

Table 1 presents the bulk density (ρ_b), skeletal density (ρ_s), linear shrinkage and porosity (ϕ) of the aerogels. The bulk densities of the as-prepared aerogels ranged from 0.09 to 0.40 g/cm³, whereas the skeletal densities varied between 1.54 and 1.73 g/cm³. No general trend is observed in the skeletal densities with respect to the aerogel composition, although the highest density is achieved for the BT composition. Notably, the skeletal density is relatively high overall, with a significant maximum of 1.73 g/cm³. An increase in the TREOS concentration leads to a significant

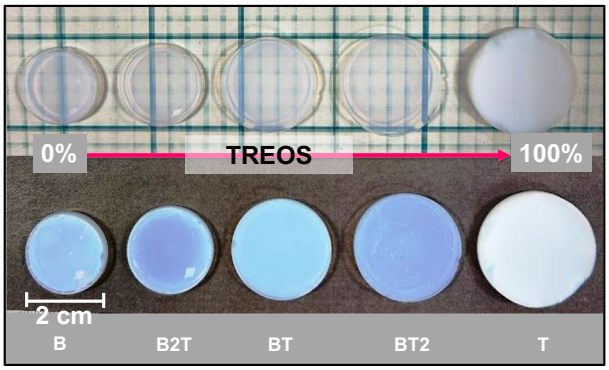

Fig. 1 Photographs depicting hybrid aerogels on white and black backgrounds. The B, B2T, BT and BT2 aerogels appear bluish on a dark background, whereas they appear transparent and slightly yellowish on a white background. The T aerogel looks white on both the dark and white backgrounds. The shrinkage of the hybrid aerogels decreases with increasing amount of TREOS

Table 1 Bulk density ρ_b, skeletal density ρ_s linear shrinkage ($\Delta L/L_0$) after gelation and supercritical drying, and porosities ϕ of hybrid aerogels

Sample	TREOS/BTEM mol ratio	ρ_b g/cm^3 ± 0.02	ρ_s g/cm^3 ± 0.01	$\Delta L/L_0$% ± 0.5	ϕ, Vol% ± 0.0
B	0	0.40	1.54	30.9	74.0
B2T	1/3	0.22	1.60	24.2	86.0
BT	1/2	0.20	1.73	18.4	88.0
BT2	2/3	0.17	1.67	15.8	90.0
T	1	0.09	1.69	8.0	95.0

decrease in the bulk density. This can be rationalized as follows: a higher TREOS content increases the degree of condensation (likely due to the low steric hindrance of the Si–H groups) in the resulting siloxane gel [30]. The high degree of crosslinking results in a robust Si-O-Si network capable of withstand drying stresses without significant shrinkage. This, in turn, accounts for the reduced drying shrinkage and the lower bulk density observed in TREOS-rich compositions. Interestingly, the bulk density and linear shrinkage are inversely related to the amount of TREOS, as depicted in Supplementary Fig. S1.

The FTIR analysis, which is presented and discussed later in this paper, further supports this argument by demonstrating a decrease in the amount of uncondensed Si-OH groups as the TREOS content increases.

3.2 Nitrogen physisorption and FTIR analysis

The isotherms, pore volume, and pore size distribution curves obtained for the hybrid aerogels are shown in Fig. 2. The isotherm and pore size distribution revealed that the aerogels possessed mesoporous characteristics with a wide range of pore diameters. The synthesized aerogels exhibit a type VIa isotherm, a characteristic feature commonly observed in mesoporous materials. All the aerogels, except B, displayed H1 hysteresis loops at relatively high pressures, suggesting the presence of large mesopores [31–33]. The pore size distribution, PSD, and curves are shown in Fig. 2b. The pore diameter of aerogel B is centered at 14 nm, whereas the B2T, BT, and BT2 aerogels predominantly have wider pore size distributions centered at 25 nm. A small number of macropores (D > 50 nm) are always present, and the number of macropores increases with increasing TREOS content (see Fig. 2b). Furthermore, the T aerogel shows a bimodal pore size distribution with two peaks, one centered at approximately 30 nm and the other at approximately 70 nm. The corresponding cumulative pore volume continues to increase, which indicates that saturation has not been achieved, suggesting the presence of larger pores (Fig. 2c). The total pore volume for T aerogels obtained from N_2 physisorption is approximately 3.97 cm^3/g (Table 2), which is lower than the volume estimated via bulk and skeletal density measurements (10.5 cm^3/g, Table S1), confirming the presence of larger pores that are not detectable via physisorption analysis.

Table 2 shows the surface area and cumulative pore volume of the preceramic aerogels under study. The specific surface area (SSA) of aerogels ranges from approximately 700 to 1400 m²/g, and the pore volume ranges from 2.00 to 10.50 cm^3/g. In our previous investigations, a specific surface area of ~1100 m²/g was measured for the aerogel from pure BTEM, which is in substantial agreement with the results presented here [26, 27]. The pore volume increases with increasing TREOS content, which is in agreement with the density measurements (Table 1); on the other hand, the SSA shows a mixed trend. The SSA evolution mirrors the simultaneous increase in pore volume and pore size as the TREOS content increases. As a result, the highest SSA is achieved for the BT composition and substantially decreases when a larger amount of TREOS is added to the system. Notably, the surface area of the synthesized aerogels stands out as one of the highest reported in the literature for silicon-based aerogels. These findings provide valuable insights into the design and optimization of hybrid gels with exceptional surface properties, offering significant potential for diverse applications across various fields.

Figure 3 shows the normalized IR spectra acquired in transmission mode for hybrid aerogels. Examination of these spectra revealed the presence of specific chemical bonds in the structure. The overall assignments of the peaks for the as-prepared aerogels are summarized in Table 3.

The main spectral feature, centered at approximately 1070 cm^{-1}, is a distinct shoulder at 1160 cm^{-1}, which is attributed to the asymmetric vibrations of Si-O-Si groups. A discernible signal within the 410–465 cm^{-1} range indicates O-Si-O bending vibrations. The absorption bands at 680 cm^{-1}

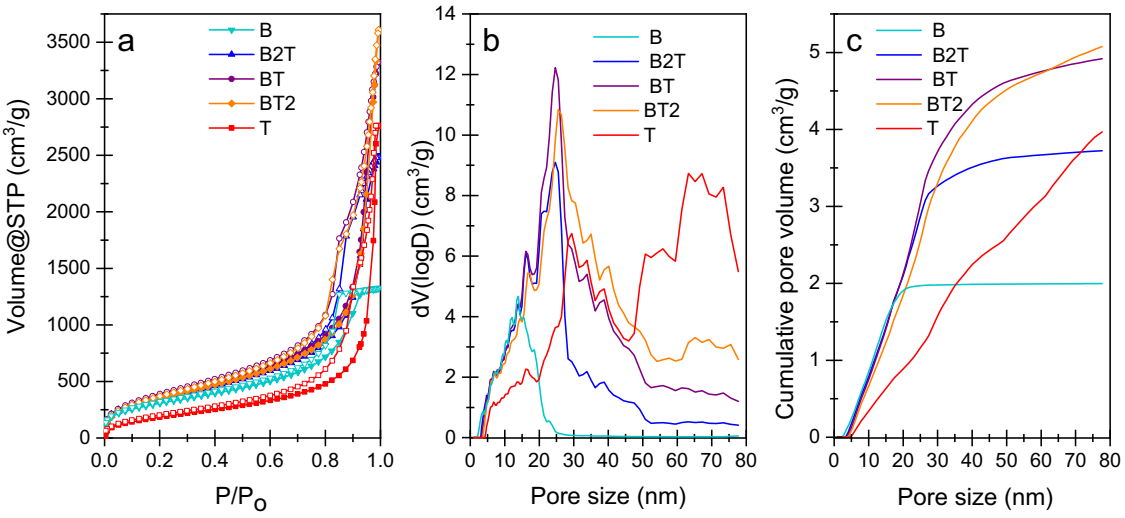

Fig. 2 **a** Nitrogen adsorption–desorption curves of the as-prepared aerogels and **b** density functional theory (DFT) density functional theory (DFT) pore size distribution. **c** Cumulative pore volume vs. pore width of the as-prepared aerogels: B, B2T, BT, and BT2 nearly reached saturation, whereas T continued to increase, suggesting the presence of larger macropores

Table 2 The specific surface area (SSA) was calculated via the BET method, and the cumulative pore volume (V) and average pore diameter (D) of the as-prepared aerogels were derived from the N_2 isotherm

Sample	TREOS/ BTEM ratio	SSA[a] m^2/g	Pore V cm^3/g	Pore D nm	ϕ_{meso} Vol%
B	0	1120	2.00	14	100
B2T	0.33	1305	3.72	25	98
BT	0.55	1395	4.92	25	94
BT2	0.76	1320	5.10	25	90
T	1.00	715	3.97	63	67

The pore size distribution characterizes pores in mesopores and macropores (up to 80 nm). where ϕ represents the percentage of mesoporosity. The molar ratio between TREOS and BTEM varies from 0 to 1

[a]Calculated via the BET method

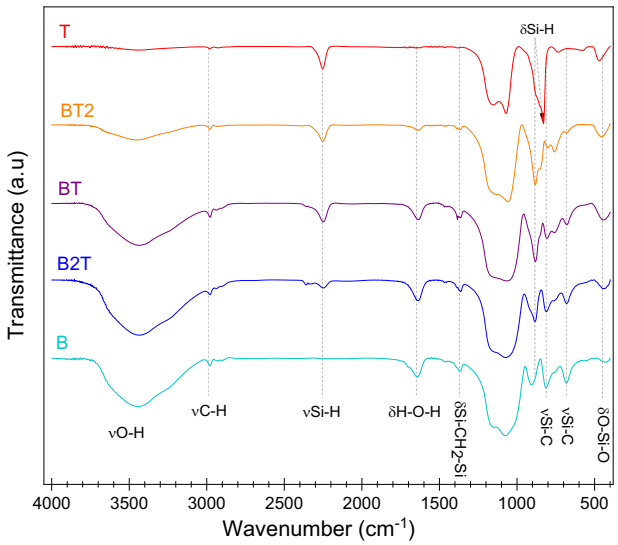

Fig. 3 Normalized FT-IR spectra of the as-prepared aerogels produced via the sol–gel process with various amounts of BTEM and TREOS

are ascribed to Si–C stretching. Interestingly, a noticeable increase in the intensity of this peak correlated with the amount of BTEM, which was in line with the amount of carbon in the hybrid aerogels.

Furthermore, bending vibrations associated with Si–H units were observed at 2250 and 880 cm^{-1} [34, 35] in the B2T, BT and BT2 aerogels. For the T aerogel, the most intense peak related to Si–H bending vibration was noted at 830 cm^{-1} [34], with a shoulder at 875 cm^{-1} and 2250 cm^{-1} (stretching). The signal that appeared from 800 to 812 cm^{-1} for the C-containing compositions BT2, BT, B2T, and B is attributed to the Si–C bond of the bridged alkoxide [36].

Most samples exhibit a prominent, broad peak at approximately 3440 cm^{-1}, attributed to the stretching O-H vibration of Si-OH and H_2O. Moreover, the absorption band at approximately 1635 cm^{-1} corresponds to the bending vibration of H_2O. These features indicate the presence of Si-OH terminal groups and adsorbed water. In contrast, aerogel T does not show peaks related to the uncondensed terminal Si-OH and adsorbed H_2O, indicating the complete condensation of silanol groups during the sol–gel process and the absence of adsorbed water molecules. Indeed, the intensities related to the vibration of Si-OH and H_2O decrease with increasing TREOS/BTEM molar ratio. Finally, the small peak at 2980 cm^{-1} is due to the different vibration modes of the C–H bonds in the -CH_x units of the residual unreacted alkoxy groups.

3.3 Scanning electron microscopy

Figure 4 shows SEM micrographs of selected aerogels (B, BT2, and T). Compared with the BT2 and T gels, the BTEM aerogel has a distinct microstructure. In fact, the B aerogel has a dense microstructure with close-packed particles, which is in agreement with the N_2 physisorption study previously reported (Fig. 2 and Table 2) and its higher bulk density among the studied aerogels (Table 1). In contrast, the BT2 and T aerogels display highly porous structures characterized by larger pores. The average pore dimension of the T aerogels was estimated to be 150 ± 50 nm via ImageJ software. Large pores (>80 nm) are challenging to detect via N_2-physisorption methods, underscoring the importance of SEM in the analysis of these materials. Thus, the SEM results align well with the density, porosity, and nitrogen adsorption data.

3.4 Thermal conductivity

Figure 5 shows the thermal conductivity of the hybrid aerogels as a function of bulk density. As the bulk density of the aerogels decreases, the overall thermal conductivity decreases due to the reduction in the solid fraction. However, when the density falls below 0.15 g/cm^3, the thermal conductivity slightly increases, which can be attributed to the higher gas thermal conduction due to macropores [9, 25, 37] within the structure. Generally, the thermal conductivity of porous materials at room temperature is influenced by both the gas and solid phases. However, when the pores fall within the mesoporous range, the contribution of the gas phase conductivity becomes negligible [8, 25, 37].

The thermal conductivity of B, B2T, and BT aerogels decreases linearly from 34.5 to 15.5 mW/mK as the bulk density decreases from 0.40 g/cm³ to 0.20 g/cm³. With respect to the N_2 sorption data, in these samples, almost all the pores are smaller than the mean free path of air at RT (~70 nm), significantly suppressing the gas phase thermal conductivity. In contrast, the presence of larger pores disrupts the linear trend in the BT2 and T samples, where approximately 7% and 65% of the pores, respectively, exceed 70 nm. Consequently, the gas-phase conductivity becomes more significant in these aerogels.

The minimum thermal conductivity of the prepared aerogels was 15 mW/mK, which is among the lowest reported values for other aerogels [28, 36, 38]. This exceptionally low thermal conductivity results from minimal heat transfer through the gas and solid phases in nanostructured materials. Specifically, pores smaller than the mean free path of gas molecules effectively reduce the gas phase thermal conductivity, whereas a low solid fraction (~10%) limits the solid phase conductivity.

The B aerogel exhibited a notable increase in thermal conductivity, reaching approximately 35 mW/mK. This sharp increase suggests that increasing the aerogel density facilitates more efficient heat conduction through the solid matrix.

Figure 5b shows the correlation between the thermal conductivity and porosity of the hybrid aerogels. It is evident that as the porosity increases, the thermal conductivity consistently decreases to 90% porosity. However, when the porosity reaches 95%, there is a slight increase, which is attributed to the occurrence of large pores.

Table 3 Bands found in the FTIR spectra of sol-gel derived aerogels

Band (cm^{-1})	Vibration	Units	Reference
3440	νO-H	≡Si-OH & H_2O	[35, 45, 46]
2980	ν_sC-H	-CH_x	[47]
2250	νSi-H	Si-H	[35, 46, 48, 49]
1640	δH-O-H	H_2O	[45, 46]
1365	δ-CH_2-	≡Si-CH_2-Si≡	[35]
1160	ν_{as}Si-O-Si	≡Si-O-Si≡	[34, 47]
1075	ν_{as}Si-O-Si	≡Si-O-Si≡	[34, 47]
900	δSi-OH	Si-OH	[50]
880	δSi-H	Si-H	[45, 46]
830	δSi-H	Si-H	[48, 51]
810	vSi-C	Si-C	[36]
680	νSi-C	Si-C	[46]
450	δO-Si-O	O-Si-O	[34, 36, 46, 47]

ν stretching vibration, ν_s symmetric stretching vibration, ν_{as} antisymmetric stretching vibration, δ deformation vibration

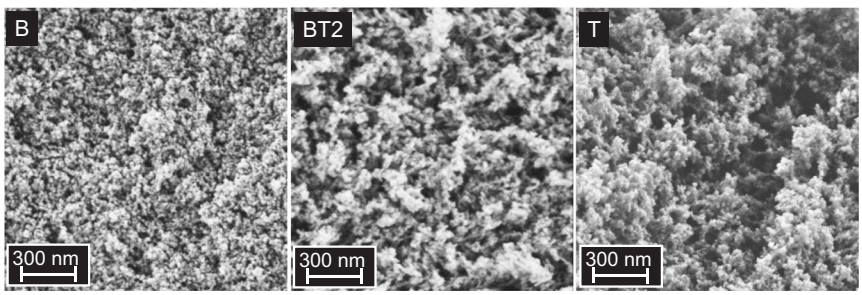

Fig. 4 Field emission scanning electron microscopy (FE-SEM) images of hybrid aerogels at room temperature (B, BT2, and T). The pore size increased with increasing amount of TREOS

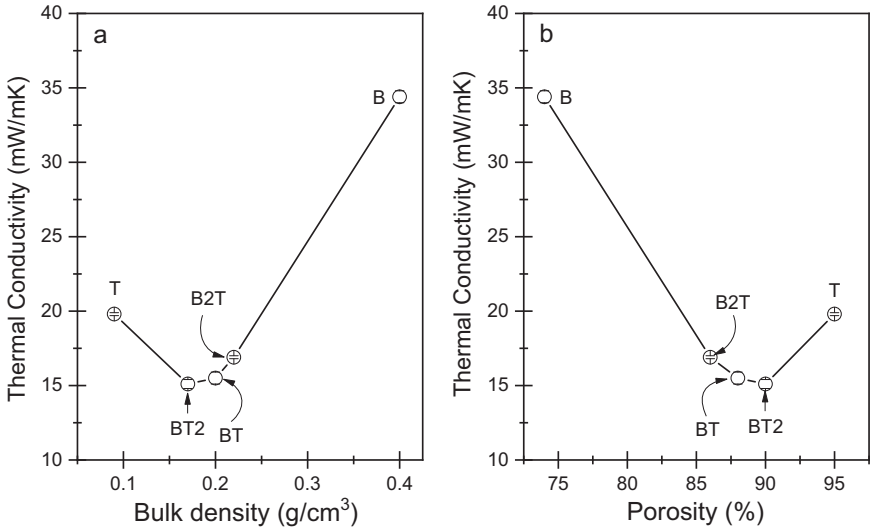

Fig. 5 Thermal conductivity of preceramic aerogels as a function of **a** bulk density and **b** porosity

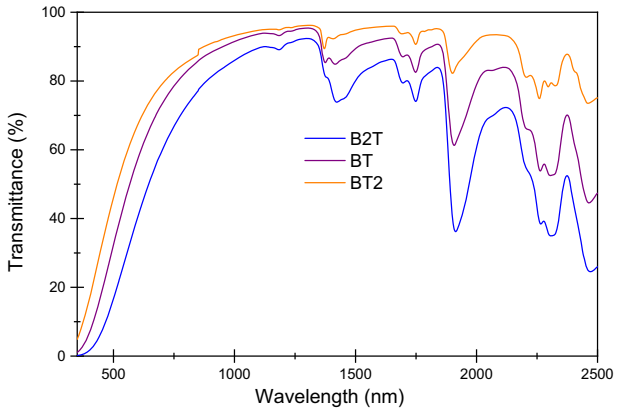

Fig. 6 Transmission spectra of the B2T, BT and BT2 aerogels (~2.50 mm thickness) at UV–Vis-NIR (350–2500 nm) wavelengths

Table 4 Comparison of the thermal and optical properties of different aerogel materials

Sample	ρ_b g/cm^3	λ_T mW/mK	T_{550} %	T_{900} %	Reference
Hybrid	0.17	15	80	96	This Study
Silica	0.17	20	98	99	[52]
Polymer	0.14	–	76		[42]
Cellulose	0.07	24	75	92	[53]
Chitosan	0.13	–	–	83	[54]

λ_T: Total thermal conductivity of porous aerogels

The transmittance of different aerogels was normalized to a thickness of 1 mm

3.5 Optical properties

Figure 6 shows the transmittance of the B2T, BT, and BT2 aerogels across the visible and near-infrared (Vis-NIR) spectra. In the visible range, the hybrid aerogels exhibit reduced transmittance, which gradually increases with increasing wavelength. This lower transmittance at shorter wavelengths is attributed to scattering. Rayleigh scattering, the primary source affecting transmittance in porous materials, occurs when colloidal particles or voids (<50 nm) interact with light of comparable dimensions—approximately one-tenth of the light wavelength [39]. As a result, the aerogels appear blue against a dark background (refer to Fig. 1).

The optical transmittances of the B2T, BT and BT2 samples (2.5 mm thick) at 780 nm are 70%, 81% and 85%, respectively. At a higher wavelength (1500 nm), the transmission increases to 80%, 89% and 95% due to reduced Rayleigh scattering, which is inversely proportional to λ^4. The BT2 sample demonstrates superior transmittance over the measured spectrum, highlighting its enhanced optical transparency. This exceptional performance is attributed to its low density, which results from minimal shrinkage during supercritical drying. Optimizing the microstructure (e.g., reducing particle and pore sizes) during the sol–gel process can further enhance the optical properties of hybrid aerogels by mitigating scattering [40].

Mesoporous aerogels are characterized by Rayleigh scattering at visible wavelengths [41, 42], and absorption becomes significant beyond a wavelength of 1000 nm [43, 44]. The transmittance measurements revealed that uncondensed Si-OH groups and water were the main absorptive species influencing the solar transmission of the studied aerogels. Notable absorption peaks were observed at approximately 1400 nm, 1700 nm, 1900 nm, and 2300 nm, which are typically associated with Si-OH and H_2O in hybrid aerogels.

Table 4 compares the optical transmittance of organic, cellulose, chitosan, hybrid and silica aerogels at 550 (visible) and 900 (IR) nm. The transmittance of these materials is normalized to an equivalent thickness of 1 mm, which is

calculated via the following relation [39, 42]:

$$T = T_0^{\frac{L}{L_0}}$$

where T_0 is the measured transmittance at thickness L_0 and T is the normalized transmittance at the equivalent thickness of 1 mm. The normalized transmittance values for the B2T, BT, and BT2 aerogels are presented in Table S2, with measurements recorded at 550 nm and 900 nm wavelengths.

This thorough analysis demonstrated that the synthesized hybrid aerogels possessed the lowest thermal conductivity and exceptionally high optical transmittance compared with those of the polymer, cellulose, and chitosan aerogels. Consequently, these aerogels have emerged as some of the most promising candidates for transparent insulation applications, including windows and Cerenkov radiators.

4 Conclusions

Hybrid silica aerogels were successfully synthesized from silicon alkoxide precursors. The amount of TREOS in the initial precursor significantly influenced the bulk density, shrinkage, and final microstructure of the aerogels. The resulting aerogels exhibited high porosities of up to 95 vol.%, BET surface area of 1400 m^2/g and a pore volume of 10.5 cm^3/g. Furthermore, the aerogels demonstrated excellent thermal insulating properties. In particular, the BT2 aerogel, with a 1:2 molar ratio between BTEM and TREOS, displayed a low thermal conductivity of 15 mW/m-K and exceeded 80% transmittance for a 1 mm thick aerogel at ≥550 nm. Thus, a combination of ultralow thermal conductivity and high transparency highlights the potential use of these hybrid silica aerogels for transparent thermal insulation applications, such as windows and solar thermal collectors.

Data availability

No datasets were generated or analysed during the current study.

Supplementary information The online version contains supplementary material available at https://doi.org/10.1007/s10971-025-06724-6.

Acknowledgements This work was supported by the European Office of Aerospace Research and Development (U.S. Air Force Office of Scientific Research) within the project "From polymers to covalent glasses (PolGla)" Award Nr. FA8655-23-1-724. The authors thank Prof. Alessandro Martucci from the University of Padova for conducting the optical transmittance measurements.

Author contributions Conceptualization, AMA, MB and GDS; Methodology, AMA, MB and GDS; Formal analysis, AMA and MC; Investigation, AMA and MC; Writing - original draft, AMA; Visualization, AMA; Writing – review & editing, AMA, MB, CV and GDS; Supervision, MB, CV and GDS; Resources, GDS; Project administration, GDS; Funding acquisition, GDS.

Funding Open access funding provided by Università degli Studi di Trento within the CRUI-CARE Agreement.

Compliance with ethical standards

Conflict of interest The authors declare no competing interests.

Publisher's note Springer Nature remains neutral with regard to jurisdictional claims in published maps and institutional affiliations.

References

1. Kistler SS (1932) Coherent expanded aerogels. J Phy Chem 36:52–64. https://doi.org/10.1021/j150331a003
2. Pierre CA, Rigacci A (2011) SiO2 Aerogels. In: Aegerter MA, Leventis N, Koebel MM (eds) Aerogels Handbook. Springer, New York, YN, pp 21–45
3. Linhares T, Pessoa De Amorim MT, Durães L (2019) Silica aerogel composites with embedded fibres: A review on their preparation, properties and applications. J Mater Chem A 7:22768–22802. https://doi.org/10.1039/c9ta04811a
4. Montes S, Maleki H (2020) Aerogels and their applications. In: Thomas S, Sunny AT, Velayudhan P (eds), Colloidal metal oxide nanoparticles: synthesis, characterization and applications. Elsevier, Amsterdam, pp 337–399
5. Karamikamkar S, Naguib HE, Park CB (2020) Advances in precursor system for silica-based aerogel production toward improved mechanical properties, customized morphology, and multifunctionality: A review. Adv Colloid Interface Sci 276:102101. https://doi.org/10.1016/j.cis.2020.102101
6. Lee KH, Arshad Z, Dahshan A, et al. (2023) Porous Aerogel Structures as Promising Materials for Photocatalysis, Thermal Insulation Textiles, and Technical Applications: A Review. Catalysts 13. https://doi.org/10.3390/catal13121498
7. Bakhori NM, Ismail Z, Hassan MZ, Dolah R (2023) Emerging Trends in Nanotechnology: Aerogel-Based Materials for Biomedical Applications. Nanomaterials 13:1–32. https://doi.org/10.3390/nano13061063
8. Hayase G, Kugimiya K, Ogawa M et al. (2014) The thermal conductivity of polymethylsilsesquioxane aerogels and xerogels with varied pore sizes for practical application as thermal superinsulators. J Mater Chem A 2:6525–6531. https://doi.org/10.1039/c3ta15094a
9. Hüsing N, Schubert U (1998) Aerogels - Airy Materials: Chemistry, Structure, and Properties. Angew Chem Int Ed 37:22–45

10. Koebel MM, Rigacci A, Achard P (2011) Aerogels for Superinsulation: A Synoptic View. In: Aegerter MA, Leventis N, Koebel MM (eds) Aerogels Handbook. Springer, New York, NY, pp 607–633
11. Li C, Zhang G, Lin L et al. (2023) Silica aerogels: from materials research to industrial applications. Int Mater Rev 68:862–900. https://doi.org/10.1080/09506608.2023.2167547
12. Mazrouei-Sebdani Z, Begum H, Schoenwald S, et al. (2021) A review on silica aerogel-based materials for acoustic applications. J Non Cryst Solids 562. https://doi.org/10.1016/j.jnoncrysol.2021.120770
13. Baetens R, Jelle BP, Gustavsen A (2011) Aerogel insulation for building applications: A state-of-the-art review. Energy Buildings 43:761–769. https://doi.org/10.1016/j.enbuild.2010.12.012
14. Cuce E, Cuce PM, Wood CJ, Riffat SB (2014) Toward aerogel based thermal superinsulation in buildings: A comprehensive review. Renew Sustain Energy Rev 34:273–299. https://doi.org/10.1016/j.rser.2014.03.017
15. Koebel M, Rigacci A, Achard P (2012) Aerogel-based thermal superinsulation: An overview. J Sol Gel Sci Technol 63:315–339
16. Abraham E, Cherpak V, Senyuk B et al. (2023) Highly transparent silanized cellulose aerogels for boosting energy efficiency of glazing in buildings. Nat Energy 8:381–396. https://doi.org/10.1038/s41560-023-01226-7
17. Strobach E, Bhatia B, Yang S, et al. (2019) High temperature stability of transparent silica aerogels for solar thermal applications. APL Mater 7. https://doi.org/10.1063/1.5109433
18. Smirnova I, Gurikov P (2018) Aerogel production: Current status, research directions, and future opportunities. J Supercrit Fluids 134:228–233. https://doi.org/10.1016/j.supflu.2017.12.037
19. Aghajamali M, Iqbal M, Purkait TK et al. (2016) Synthesis and Properties of Luminescent Silicon Nanocrystal/Silica Aerogel Hybrid Materials. Chem Mater 28:3877–3886. https://doi.org/10.1021/acs.chemmater.6b01114
20. Li Z, Zhao S, Koebel MM, Malfait WJ (2020) Silica aerogels with tailored chemical functionality. Mater Des 193:108833. https://doi.org/10.1016/j.matdes.2020.108833
21. Meti P, Mahadik DB, Lee KY et al. (2022) Overview of organic–inorganic hybrid silica aerogels: Progress and perspectives. Mater Des 222:111091. https://doi.org/10.1016/j.matdes.2022.111091
22. Ueoka R, Hara Y, Maeno A, et al. (2024) Unusual flexibility of transparent poly (methylsilsesquioxane) aerogels by surfactant-induced mesoscopic fiber-like assembly. Nat Commun 15. https://doi.org/10.1038/s41467-024-44713-5
23. An L, Li Z, Guo Z et al. (2022) Transparent thermal insulation ceramic aerogel materials for solar thermal conversion. Nanoscale Adv 4:4291–4295. https://doi.org/10.1039/d2na00412g
24. Wu L, Zhao B, Gao D, et al. (2023) Solar transparent and thermally insulated silica aerogel for efficiency improvement of photovoltaic/thermal collectors. Carbon Neutrality 2. https://doi.org/10.1007/s43979-023-00046-8
25. Lu X, Arduini-Schuster MC, Kuhn J et al. (1992) Thermal Conductivity of Monolithic Organic Aerogels. Science 255:971–972. https://doi.org/10.1126/science.255.5047.971
26. Abebe AM, Soraru GD, Thothadri G et al. (2022) Synthesis and Characterization of High Surface Area Transparent SiOC Aerogels from Hybrid Silicon Alkoxide: A Comparison between Ambient Pressure and Supercritical Drying. Materials 15:1277. https://doi.org/10.3390/ma15041277
27. Dirè S, Borovin E, Narisawa M, Sorarù GD (2015) Synthesis and characterization of the first transparent silicon oxycarbide aerogel obtained through H2 decarbonization. J Mater Chem A 3:24405–24413. https://doi.org/10.1039/c5ta06669g
28. Zu G, Shimizu T, Kanamori K et al. (2018) Transparent, Superflexible Doubly Cross-Linked Polyvinylpolymethylsiloxane Aerogel Superinsulators via Ambient Pressure Drying. ACS Nano 12:521–532. https://doi.org/10.1021/acsnano.7b07117
29. Mandal C, Donthula S, Soni R et al. (2019) Light scattering and haze in TMOS-co-APTES silica aerogels. J Sol Gel Sci Technol 90:127–139. https://doi.org/10.1007/s10971-018-4801-0
30. Sorarù GD (1994) Silicon oxycarbide glasses from gels. J Sol Gel Sci Technol 2:843–848. https://doi.org/10.1007/BF00486362
31. Sotomayor FJ, Cychosz KA, Thommes M (2018) Characterization of Micro/Mesoporous Materials by Physisorption: Concepts and Case Studies. Acc Mater Surf Res 3:34–50
32. Schlumberger C, Thommes M (2021) Characterization of Hierarchically Ordered Porous Materials by Physisorption and Mercury Porosimetry—A Tutorial Review. Adv Mater Interfaces 8. https://doi.org/10.1002/admi.202002181
33. Cychosz KA, Guillet-Nicolas R, García-Martínez J, Thommes M (2017) Recent advances in the textural characterization of hierarchically structured nanoporous materials. Chem Soc Rev 46:389–414. https://doi.org/10.1039/c6cs00391e
34. Sorarù GD, D'Andrea G, Campostrini R, Babonneau F (1995) Characterization of methyl-substituted silica gels with Si-H functionalities. J Mater Chem 5:1363–1374. https://doi.org/10.1039/JM9950501363
35. Niemiec W, Szczygieł P, Jeleń P, Handke M (2018) IR investigation on silicon oxycarbide structure obtained from precursors with 1:1 silicon to carbon atoms ratio and various carbon atoms distribution. J Mol Struct 1164:217–226. https://doi.org/10.1016/j.molstruc.2018.03.046
36. Feng J, Feng J, Xiao Y, Jiang Y (2015) Synthesis, structure, and properties of silicon oxycarbide aerogels derived from tetraethylortosilicate /polydimethylsiloxane. Ceram Int 41:5281–5286. https://doi.org/10.1016/j.ceramint.2014.11.111
37. Lu X, Caps R, Fricke J et al. (1995) Correlation between structure and thermal conductivity of organic aerogels. J Non Cryst Solids 188:226–234. https://doi.org/10.1016/0022-3093(95)00191-3
38. Zu G, Kanamori K, Shimizu T et al. (2018) Versatile Double-Cross-Linking Approach to Transparent, Machinable, Supercompressible, Highly Bendable Aerogel Thermal Superinsulators. Chem Mater 30:2759–2770. https://doi.org/10.1021/acs.chemmater.8b00563
39. Merillas B, Martín-De León J, Villafañe F, Rodríguez-Pérez MÁ (2022) Optical Properties of Polyisocyanurate–Polyurethane Aerogels: Study of the Scattering Mechanisms. Nanomaterials 12. https://doi.org/10.3390/nano12091522
40. Zhao L, Bhatia B, Zhang L et al. (2020) A Passive High-Temperature High-Pressure Solar Steam Generator for Medical Sterilization. Joule 4:2733–2745. https://doi.org/10.1016/j.joule.2020.10.007
41. Jones AR (1999) Light scattering for particle characterization. J Non Cryst Solids 25:1–53. https://doi.org/10.1016/S0360-1285(98)00017-3
42. Merillas B, Martín-De León J, Villafañe F, Rodríguez-Pérez MA (2021) Transparent Polyisocyanurate-Polyurethane-Based Aerogels: Key Aspects on the Synthesis and Their Porous Structures. ACS App Polym Mater 3:4607–4615. https://doi.org/10.1021/acsapm.1c00712
43. Fiorini CV, Merli F, Belloni E, et al. (2023) Long-Term Performance of Monolithic Silica Aerogel with Different Hydrophobicities: Physical and Color Rendering Properties after an Accelerated Aging Process. Gels 9. https://doi.org/10.3390/gels9030210
44. McEnaney K, Weinstein L, Kraemer D et al. (2017) Aerogel-based solar thermal receivers. Nano Energy 40:180–186. https://doi.org/10.1016/j.nanoen.2017.08.006
45. Kolář F, Machovič V, Svítilová J, Borecká L (2004) Structural characterization and thermal oxidation resistance of silicon oxycarbides produced by polysiloxane pyrolysis. Mater Chem Phys 86:88–98. https://doi.org/10.1016/j.matchemphys.2004.02.011

46. Chomel AD, Dempsey P, Latournerie J et al. (2005) Gel to glass transformation of methyltriethoxysilane: A silicon oxycarbide glass precursor investigated using vibrational spectroscopy. Chem Mater 17:4468–4473. https://doi.org/10.1021/cm050501p
47. Brigo L, Faustini M, Pistore A et al. (2016) Porous inorganic thin films from bridged silsesquioxane sol–gel precursors. J Non Cryst Solids 432:399–405. https://doi.org/10.1016/j.jnoncrysol.2015.10.041
48. Karakuscu A, Guider R, Pavesi L, Sorarù GD (2009) White luminescence from sol-gel-derived SiOC thin films. J Am Ceram Soc 92:2969–2974. https://doi.org/10.1111/j.1551-2916.2009.03343.x
49. Sorarù GD, Karakuscu A, Boissiere C, Babonneau F (2012) On the shrinkage during pyrolysis of thin films and bulk components: The case of a hybrid silica gel precursor for SiOC glasses. J Eur Ceram Soc 32:627–632. https://doi.org/10.1016/j.jeurceramsoc.2011.10.004
50. Sorarù GD, Liu Q, Interrante LV, Apple T (1998) Role of precursor molecular structure on the microstructure and high temperature stability of silicon oxycarbide glasses derived from methylene-bridged polycarbosilanes. Chem Mater 10:4047–4054. https://doi.org/10.1021/cm9804719
51. Sorarù GD, D'Andrea G, Campostrini R et al. (1995) Structural Characterization and High-Temperature Behavior of Silicon Oxycarbide Glasses Prepared from Sol-Gel Precursors Containing Si-H Bonds. J Am Ceram Soc 78:379–387. https://doi.org/10.1111/j.1151-2916.1995.tb08811.x
52. Strobach E, Bhatia B, Yang S et al. (2017) High temperature annealing for structural optimization of silica aerogels in solar thermal applications. J Non Cryst Solids 462:72–77. https://doi.org/10.1016/j.jnoncrysol.2017.02.009
53. Ayadi F, Martín-García B, Colombo M et al. (2016) Mechanically flexible and optically transparent three-dimensional nanofibrous amorphous aerocellulose. Carbohydrate Polymers 149:217–223. https://doi.org/10.1016/j.carbpol.2016.04.103
54. Takeshita S, Yoda S (2015) Chitosan Aerogels: Transparent, Flexible Thermal Insulators. Chem Mater 27:7569–7572. https://doi.org/10.1021/acs.chemmater.5b03610